Skin Cooling of Turbine Airfoils by Single Wall Effusion: Part I—Reduced Order Modeling

Yair Lange
Faculty of Aerospace Engineering,
Turbo & Jet Engine Laboratory,
Technion—Israel Institute of Technology,
Haifa 32000, Israel
e-mail: ylange@alumni.technion.ac.il

S. Fatih Kırmızıgöl
Faculty of Engineering and Architecture,
Mechanical Engineering Laboratory,
İzmir Katip çelebi University,
İzmir 35620, Turkey
e-mail: fatihk@esalba.com

Sercan Acarer
Associate Professor
Faculty of Engineering and Architecture,
Mechanical Engineering Department,
İzmir Katip çelebi University,
İzmir 35620, Turkey
e-mail: sercan.acarer@ikcu.edu.tr

Beni Cukurel[1]
Mem. ASME
Associate Professor
Faculty of Aerospace Engineering,
Turbo & Jet Engine Laboratory,
Technion—Israel Institute of Technology,
Haifa 32000, Israel
e-mails: bcukurel@technion.ac.il;
beni@cukurel.org

A quasi-1D conjugate reduced order model (ROM) is developed to capture aero-thermal physics of effusion cooling in turbine airfoils. This framework explicitly considers the coolant supply from the leading edge and its distribution to both suction and pressure sides, the internal boundary layer flow between the shell and the inner core, the hole flow, the conduction on the solid walls, as well as the external film coverage. The solid temperature is allowed to vary both in metal shell thickness and the streamwise directions. Empirical correlations are employed to model pressure loss and heat transfer in the internal sections. Compound effect of multiple effusion cooling rows are utilized to capture cooling effectiveness and the heat load. Influence of mainstream static pressure, varying blowing ratios, hole's diameter, hole's pitch, coolant total pressure, and total temperature distributions along streamwise direction are taken into account. In Part I, the development and validation of the model is presented, which is shown to be capable of capturing complex internal aero-thermal physics of a turbine airfoil. Film coverage capability is separately validated successfully against available flat plate experimental data, with one case including internal channel and metal conduction. In Part II of this work, effusion cooling configuration is applied over an entire micro turbine vane and an exemplary optimization is carried out in the design space to minimize coolant flow while retaining metal temperature and its gradient below some limits. It is shown in the two-part work that the developed model is suitable for parametric studies of single-wall effusion turbine cooling such that comparative accuracy is obtained at a computational time 10^5 times lower than computational fluid dynamics (CFD) on a whole turbine vane/blade. Together, these two papers are intended to present, validate, and optimize the ROM for skin cooling in turbine airfoils by single-wall effusion. [DOI: 10.1115/1.4056876]

Keywords: effusion cooling, skin cooling, reduced order model, preliminary design tool, gas turbine, aerospace heat transfer, porous media, thermal systems

Introduction

There is an ever-growing demand for better turbine cooling techniques to prevent the blades from reaching their structural material limits. Among the external cooling methodologies, film cooling is the most widely used. When designing turbine cooling systems, assessment of film cooling effectiveness is important towards quantifying the heat flux from the hot gas path to the blade material. Hence, large amounts of scientific research on cooling effectiveness exist to predict flow characteristics.

Film Cooling. Considering the baseline model of round film cooling hole on a flat plate, the correlation developed by L'Ecuyer and Soechting accounts for three different flow phenomena (mass addition, mixing, and penetration) related to velocity ratios [1]. This model requires information regarding amplitude and downstream location of peak effectiveness. Building upon the Stone and Goldstein correlation [2], Boyle and Ameri [3] presented an equation accounting for the freestream turbulence effects, as a function of turbulence intensity, injection angle, and spacing. One of the most widely used film cooling effectiveness correlations was offered by Colban et al. [4]. This comprehensive work suggested a three-coefficient cooling effectiveness model based on 57 datasets, thus providing an expanded parameter range and better accuracy than previous correlations, with particular prediction benefit in the leading edge region [5].

In case of compound cooling, modeling can be challenging when including the mixing effects. A well-known technique to simulate the performance of multiple injection stations is the Sellers model [6], which relies on single hole data and can be used for calculating adiabatic film cooling effectiveness. This compound cooling model was improved by applying energy conservation between the different film cooling layers [7], which results in improved accuracy where previous methods reported deviations. More recently, this theory was expanded to cooling holes with multiple coolant temperatures, as depicted by Fuqua and Rutledge [8].

For designs employing film cooling, being able to predict the external heat transfer coefficient (HTC) augmentation is important as well. Attributed to jet and mainstream interaction, increasing blowing ratio is found to increase HTC significantly [9]. In his experimental and numerical heat transfer analysis with full coverage film cooling holes, Hodges [10] found that augmentation of HTC is amplified along the curve-linear direction, as more coolant is introduced into the mainstream.

Another challenge in implementation of film cooling in turbine blades is associated with the coupling of the aero-thermal performance of internal and external passages. From the aerodynamic perspective, the coolant pressure losses through the hole are typically represented by the discharge coefficient, which is defined as the ratio between real and theoretical mass through-hole mass flowrates. Among all the factors affecting discharge coefficient in full coverage cooling arrays, hole Reynolds number is found to be the dominant parameter [11], while hole length-to-diameter ratio has a relatively

---

[1]Corresponding author.

small impact and crossflow, compressibility and wall friction effects are minor correction factors. From the internal channel heat transfer perspective, suction of the fluid into the hole has an impact on local Nusselt number distributions. With respect to suction ratio (the ratio between hole velocity and channel velocity) and channel Reynolds number, this local heat transfer coefficient has been correlated for smooth and turbulated passages [12,13], respectively. Increasing suction ratio results in higher augmentation factor at the near hole region for 90 deg ejection angle [14].

From Macroscale to Microscale. A considerable amount of coolant air flow is needed in conventional film cooling, and thus a penalty on the thermodynamic cycle efficiency and aerodynamic losses are inevitable. Moreover, when distinct holes are introduced on the blade or vane surface, the temperature gradients are unavoidable, limiting the life of the components. Impact of thermal stress on lifetime was shown in a combustion liner investigation [15]. In highly cooled blades with film cooling, the near hole regions have significant temperature gradients, and as a function of thermal expansion mismatch and coating thickness, it even leads to cracking of thermal barrier coatings [16–18]. Therefore, decreasing the nominal metal temperatures and their spatial gradients will result in better resistance to creep and low cycle fatigue.

In addition, when looking at the variety of micro turbine designs, both in the field of propulsion and in the power generation sector, the available units do not use externally cooled blades or vanes since conventional film cooling technologies are highly unsuitable under spatial constraints. For example, the film cooling hole diameter is generally of the ~1 mm order, whereas micro turbine chord is usually only one order of magnitude larger. In an attempt to alleviate this issue, there is a big push to go from macro- to micro-cooling technologies [19,20]. Effusion cooling (EC) strategies incorporate an array of micro-holes, flowing through which the coolant covers the surface of the blade.

However, computational fluid dynamics (CFD) simulations of the micro-cooling geometries are computationally expensive, especially when accounting the coupled nature of external convection, conduction, and internal convection. In particular, the simulation cost is mainly associated with the discrepancy of feature size between holes, internal channel and mainstream passage, and the propagation time of thermal fluxes. Furthermore, although the linear periodicity can be satisfied in case of a constant hole size and pitch distribution, for varying hole diameter and pitch, the entire flow passage needs to be simulated, which greatly amplifies the computational cost and ultimately becomes impractical.

Addressing this issue, there have been several investigations on external effusion cooling coverage in benchmark geometries. A correlative analysis was conducted on a flat effusion plate [21], validating a simplified numerical two-dimensional conjugate approach through comparison with experimental results of effectiveness on a plate. The findings reflected that smaller holes with constant pitch to diameter ratio give higher effectiveness. This analysis showed dependence of the overall effectiveness on external heat transfer coefficient, while using a fully turbulent correlation to calculate it. Although the accuracy of employing film cooling effectiveness correlations in effusion surfaces is not obvious, good agreement was achieved between the predictions and the experiments. Yang and Rao [22] considered a similar case and trained an artificial intelligence (AI)-based reduced order model (ROM) using CFD and showed that the convolution method can be trained with relatively small amount of data. Another study demonstrated mass and energy source approach to model effusion holes in a large eddy simulation framework without meshing holes [23]. Finally, Qu et al. [24] have experimentally shown that some cooling effectiveness improvement potential exist when slot blowing is used in conjunction with effusion holes. Nevertheless, these three works concentrated on cases representing a combustion chamber, i.e., low Mach number and uniform pressure for the external flow.

Motivation. Beyond correlative works associated with external cooling contributing to the database of performance metrics and their dependence to a range of parameters, to the authors' best knowledge, a conjugate reduced order model that predicts the performance of the single-wall effusion cooling scheme (also known as "skin cooling" [19]) in turbine applications does not exist. In particular, for the basic effusion cooling configuration, beyond the challenges associated with other micro-cooling technologies, momentum and thermal boundary layer development associated with the internal channel flow between the inner solid core and outer shell needs to be considered. Moreover, the spatial distribution of hole mass flowrate and entry temperature must be taken into account. Even though simplified 3D or 1D approaches on double wall cooling have been studied recently [25,26], single-wall skin cooling is a simple and strong alternative to double wall cooling systems for small-scale turbines and more research is needed in this area.

Along these lines, the current work aims to fill this gap by developing a well-tailored reduced order model considering airfoil representative single-wall skin cooling in which quasi-2D conduction, coolant distribution to suction-pressure sides, internal momentum-thermal boundary layer, and external film coverage modeling are included in a rapid algebraic model framework, as demonstrated in Table 1.

Due to disparity of geometric scales with feature size as small as 50 μm, the CPU time of a conjugate heat transfer (CHT) Reynolds-averaged Navier–Stokes (RANS) CFD simulation with effusion cooling (with approximately requiring 700 million mesh elements) on a whole turbine blade/vane would approximately take ~1 month on a typical workstation (24 modern Xeon cores); therefore, this type of approach is inhibitive for optimization and preliminary design. On the contrary, it is shown in this two-part work that the developed model is suitable for parametric studies of single-wall effusion turbine cooling such that comparative accuracy is obtained at a computational time 10^5 times lower than CFD on a whole turbine vane/blade. The application of this reduced order model as a preliminary design tool for skin cooled turbine airfoils is discussed in Part II of this paper.

Reduced Order Effusion Cooling Model. The reduced order model in this work is composed of a CHT module, which solves the shell internal and the hole through flows, as well as conduction in the shell, and an EC module that considers the compound effectiveness on the external surface arising from the coolant buildup.

For a given coolant plenum pressure and temperature, the streamwise distributions of local static pressure and adiabatic wall heat transfer coefficient over the blade are inputs to the algorithm. The code is initialized with a guess on both metal temperature and external heat flux load. Then, the CHT module calculates all the aerothermal quantities (pressure, temperature, and velocity fields) in both the internal passage and the hole through-flow domains. Once the convective heat fluxes in all wetted surfaces are computed, metal energy balance is used to capture the conduction in the streamwise (including from trailing edge) and wall thickness directions. The resultant metal temperature distributions are the output of the system of equations. In the following, EC module focuses on the shell external surface of the airfoil and uses energy conservation between the coolant film layers to account for the additive compound effect stemming from multiple injection holes. The uncooled blade heat transfer coefficient is corrected for the augmentation resulting from the film cooling injection. Then, the revised external heat flux distribution is fed back into the CHT module, initiated with a new wall temperature distribution guess. The iterations continue until convergence is achieved on the local external heat flux values between the loops. The algorithm is programed in MATH-WORKS MATLAB 2020B and summarized in a flowchart in Fig. 1.

Conjugate Heat Transfer Module. This section describes the detailed methodology and equations that constitute the conjugate

Table 1 Comparison of simplified modeling approaches for effusion cooling

Reference	Internal flow	Metal conduction	External flow	Type	Flow fidelity	Validation
Arcangeli et al. (2008) [21]	None (reservoir)	2D	Flat plate, low Mach	Single wall	1D ROM	Exp.
Yang and Rao (2019) [22]		No		Single wall	1D AI-based ROM	CFD/Exp.
Gottiparthi et al. (2019) [23]		3D		Single wall	Simp. 3D	Exp./CFD
Murray et al., 2019 [25]		3D	Vane representative	Double wall	Simp. 3D	Exp./CFD
Murray et al. (2019) [26]		1D		Double wall	1D ROM	Exp./CFD
Present work	Yes, boundary layers	Quasi-2D		Single wall	1D ROM	Exp./CFD

heat transfer module. The flowchart, outlining the order of information transfer, is outlined in Fig. 2. The geometric inputs to the solver are internal channel length, shell thickness, passage thickness, hole spacing, and hole diameter. The set of equations describing conjugate heat transfer are applied for both pressure and suction sides separately, while metal temperature information at the leading and trailing edges is transferred between the two sides of the blade to ensure continuity.

Quasi-2D modeling of the metal temperature, which considers temperature variation both in streamwise and wall-normal directions, is taken into account. The term "quasi" is used because a limited number of nodes is employed: shell inner, shell center, and shell outer as well as the center nodes of the neighboring shell (metal) segments.

The module is initialized by uniform internal channel and hole outlet total pressures and temperatures $P_{0,\mathrm{ch}}(x)$, $P_{0,\mathrm{eo}}(x)$, $T_{0,\mathrm{ch}}(x)$, $T_{0,\mathrm{eo}}(x)$ as well as external (vane/blade surface) metal temperature distribution T_w.

The internal channel and hole flow are solved through three types of local control volumes, depicted in Fig. 3. CV_1 signifies the flow inside the internal channel undisturbed by the suction of the

neighboring hole, whereas CV_2 is associated with the part of the fluid that is purged through the hole. The aerodynamics of the internal channel flow (CV_1 and CV_2) are solved in an iterative manner, converging hole exit and internal channel total pressure and temperatures. The through flow inside the hole (CV_3) is considered with the external static pressure distribution, coolant's hole inlet total pressure and temperatures. Physical properties of the internal channel flow are stored at each streamwise hole location. Each hole domain inlet conditions are the outlet of the previous domain, defining internal channel stagnation properties and wall temperature. Once the flow circuit is established with the calculated internal channel and hole heat fluxes, the external heat flux, and the conduction losses to the neighboring elements, energy balance is applied on each discrete solid element of the shell encompassing the hole domain (CV_4 in Fig. 3). This enables computation of local shell metal temperatures that are updated in the module, which in turn affects hole exit total temperature. The entire loop in Fig. 2 is iterated for convergence in internal channel and hole outlet total pressures, fluid density, and in-metal temperatures with thresholds of 0.1%, 0.01% and 0.0001%, respectively. These values are chosen to ensure convergence, while preserving a relatively short runtime.

In each section of interest, the calculation starts at effusion hole outlet (CV_3), where the total pressure is initialized to be equal to
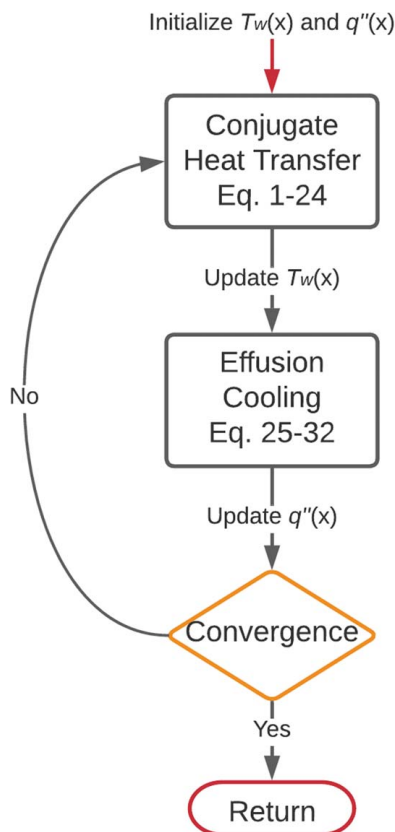

Fig. 1 Reduced order model flowchart for turbine blade equipped with basic effusion cooling. CHT: Eqs. (1)–(24), external effusion cooling: Eqs. (25)–(32).
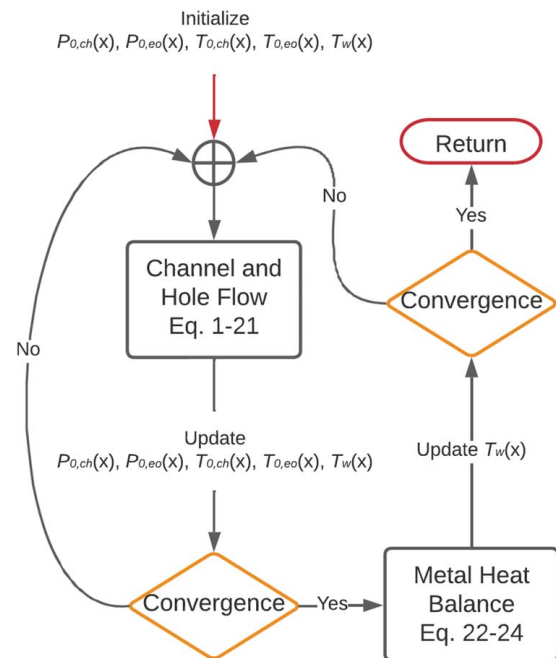

Fig. 2 Conjugate heat transfer module of the reduced order effusion-cooled turbine model. Internal channel and hole flows: Eqs. (1)–(21), metal heat balance: Eqs. (22)–(24). Subscript "0" denotes stagnation conditions, "ch" denotes internal channel, "eo" denotes effusion hole outlet, and "w" denotes external wall of the turbine.
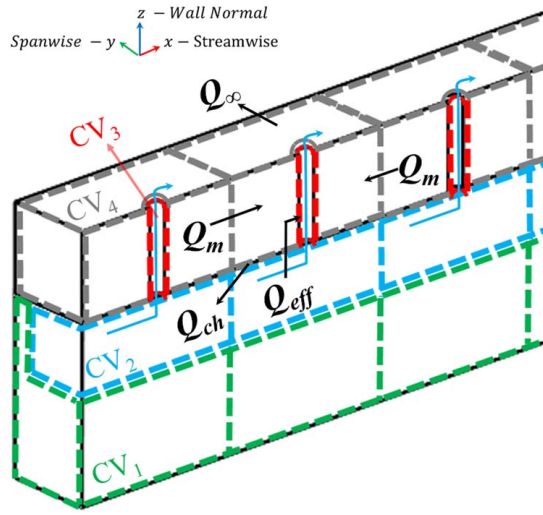
Fig. 3 Control volume (CV) definitions of conjugate heat transfer module: CV1 for the part of the internal channel flow which is undisturbed by the suction of the neighboring hole, CV2 for the remaining part of the internal channel flow, which is purged through the downstream hole, CV3 for the through flow inside the hole and CV4 for the energy balance applied on each discrete solid element of the shell encompassing the hole domain. Subscripts "ch, eff, m, and ∞" stand for "internal channel, effusion, metal, and external flow," respectively.

the coolant plenum total pressure ($P_{0,\mathrm{eo}} = P_{0_{C,i}}$). Mach numbers and static temperatures are extracted from the following isentropic relations:

$$M_{\mathrm{eo}} = k_v \sqrt{\frac{2}{\gamma - 1} \left((P_{s,\mathrm{eo}}/P_{0,\mathrm{eo}})^{(1-\gamma/\gamma)} - 1 \right)} \tag{1}$$

$$T_{s,\mathrm{eo}} = T_{0,\mathrm{eo}} (P_{s,\mathrm{eo}}/P_{0,\mathrm{eo}})^{(\gamma-1)/\gamma}$$

where k_v is an empirical viscous correction coefficient equal to 0.94. Also influenced by the low Reynolds number of $\sim$500, this correction accounts for the highly non-uniform flow region at the vicinity of the hole exit, where average of local Mach and Mach calculated from averaged pressures differs.

In the following, effusion holes exit conditions and mass flowrates are calculated using compressible ideal gas relations:

$$u_{\mathrm{eo}} = M_{\mathrm{eo}} \sqrt{\gamma R T_{s,\mathrm{eo}}}, \quad \rho_{\mathrm{eo}} = \frac{P_{s,\mathrm{eo}}}{R T_{s,\mathrm{eo}}} \tag{2}$$

$$\dot{m}_{\mathrm{eo}} = \rho_{\mathrm{eo}} u_{\mathrm{eo}} A_{\mathrm{act}}, \quad A_{\mathrm{act}} = \pi (D/2 - \delta^\star_{\mathrm{eo}})^2$$

The effective hole area A_{act} accounts for boundary blockage, according to a modified Blasius solution [27], which is intended to compensate for the compressibility effects and the inherently more complex flow structures. In this scenario, the displacement thickness is calculated using

$$\delta^\star_{\mathrm{eo}} = k_{\delta^\star} \frac{L}{\sqrt{\mathrm{Re}_L}} \tag{3}$$

where $k_{\delta^\star}$ is fitted empirically using a two-term power series model:

$$k_{\delta^\star} = c_1 (\mathrm{Re}_{\mathrm{pit}}/\mathrm{Re}_{\mathrm{eo}})^{c_2} + c_3 \tag{4}$$
$$c_1 = -0.213, \qquad c_2 = -0.404, \qquad c_3 = 0.803$$

In the range of 0.7–0.75 for most relevant conditions, $k_{\delta^\star}$ varies according to the ratio of the Reynolds numbers based on pitch and hole diameter, signifying that higher inertia in the internal channel with respect to the hole increases the blockage.

After the through-hole flow computation, the internal channel flow (CV$_1$ and CV$_2$) is characterized using the following relations:

$$u_{\mathrm{ch}} = \frac{\dot{m}_{\mathrm{ch}}}{\rho_{\mathrm{ch}} A_{\mathrm{ch}}}, \quad T_{s,\mathrm{ch}} = T_{0,\mathrm{ch}} - u_{\mathrm{ch}}^2/2C_p$$

$$M_{\mathrm{ch}} = u_{\mathrm{ch}}/\sqrt{\gamma R T_{s,\mathrm{ch}}}$$

$$P_{s,\mathrm{ch}} = P_{0,\mathrm{ch}} (T_{s,\mathrm{ch}}/T_{0,\mathrm{ch}})^{\gamma/(\gamma-1)} \tag{5}$$

$$\rho_{\mathrm{ch}} = \frac{P_{s,\mathrm{ch}}}{R T_{s,\mathrm{ch}}}$$

The channel effective cross-sectional area is calculated using Blasius solution:

$$A_{\mathrm{ch}} = (t - \delta^\star_{\mathrm{ch}})\mathrm{pit}, \quad \delta^\star_{\mathrm{ch}} = 1.72 \frac{\mathrm{pit}}{\sqrt{\mathrm{Re}_{\mathrm{pit}}}} \tag{6}$$

The flow domain is calculated from the plenum in the leading edge towards the last hole in the trailing edge on the suction and pressure sides independently. Locally, the channel mass flowrate is determined from conservation of mass, by summing all the effusion hole ejection downstream of each section of interest. Equation (5) requires iterations as the static properties depend on the mass flowrate through the channel. Then, pressure loss and heat transfer correlations are used to calculate total pressures and temperatures throughout the channel and the effusion holes.

The principal pressure loss mechanism inside the effusion hole (CV$_3$) is captured by the discharge coefficient (C_D). Recreated from an experimental study on the subject [11], Fig. 4 presents the discharge coefficients as a function of hole Reynolds number in two distinct hole length-to-diameter ratios (L/D), 4.6 and 9.94. The discharge coefficient values are interpolated for intermediate L/D ratios and the available experimental data show that C_D is only a function of Re for L/D below 4.6 [11]. Then, pressure loss in effusion hole can be calculated as

$$\Delta P_{0,\mathrm{eff}} = K_T \left(\frac{1}{2} \rho_{\mathrm{eo}} u_{\mathrm{eo}}^2 \right)$$

$$K_T = \frac{K_{CD}^2}{C_D^2}, \quad C_D = f\left(\mathrm{Re}_{\mathrm{eo}}, \frac{L}{D} \right) \tag{7}$$

$$K_{CD} = 1/(-2.33 \cdot 10^{-15} \mathrm{Re}_{\mathrm{ch}}^{3.72} + 1.8)$$

where K_{CD} is a compensating factor between the relation of minor loss coefficient (K_T) and discharge coefficient (C_D), similar to that
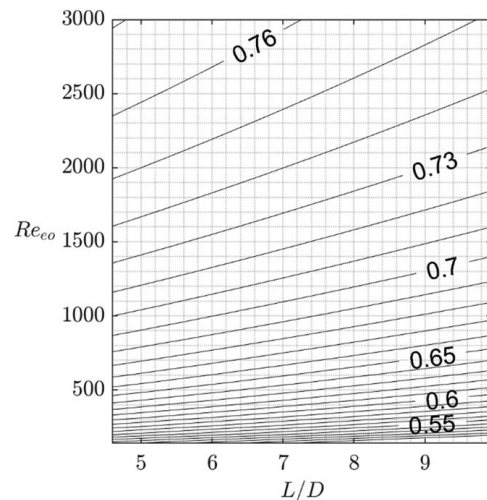

Fig. 4 Experimental discharge coefficient data CD as a function of hole Reynolds number and length to diameter ratio (interpolated data based on reconstruction from Ref. [11])

defined in Ref. [28] but correlated to the current problem. Re_{ch} and Re_{eo} imply Reynolds numbers based on local hydraulic diameters of the internal channel and the holes, respectively. As the channel Reynolds number raises, the pressure drop through the holes increases and more viscous losses are subjected to the correlation.

Considering the internal channel flow in CV_1 and CV_2, the pressure losses are based on friction coefficient f in a fully developed flow [29]:

$$\Delta P_{0,\text{fr}} = \frac{1}{2} f \frac{\text{pit}}{D} \rho_{\text{ch}} u_{\text{ch}}^2$$

$$\frac{1}{\sqrt{f}} = -1.8 \log \left[\frac{6.9}{Re_{\text{ch}}} + \left(\frac{\varepsilon/D_{\text{hyd}}}{3.7} \right)^{1.11} \right] \tag{8}$$

where the friction roughness is taken to be $\varepsilon = 0.07$ mm. In casting processes, surface roughness of $70\,\mu m$ is typical [30]. Moreover, even for more advanced manufacturing processes such as laser powder bed fusion, the laser spot diameter and/or the hatching distance can be of this magnitude [31]. Then, the flow can be considered in completely rough regime, where all the protrusions extend over the laminar layer and generate additional resistance against the flow and the friction factor depends on the surface roughness [32].

In order to reconcile the exit pressure difference between the pressure and suction sides of the blade, a porous media can be used in the leading edge of the suction side as a local blockage mechanism, preventing blow off further downstream. The Forchheimer equation is used for calculating the pressure drop associated with porous media:

$$\Delta P_{0,\text{porous}} = [(\mu/k_d)u_{\text{ch}} + \beta\rho u_{\text{ch}}^2]\Delta x \tag{9}$$

The Darcy's permeability factor k_d and inertial resistance β are $1.413e^{-10}$ and $5.342e^4$, respectively, which are calculated using the linear correlation coefficients of material 1 in Table III of Ref. [33] ($A = 202$, $B = 2.77$), with porosity value of $\varepsilon = 0.455$ and equivalent mean sphere diameter of $D_{\text{eq}} = 3 \times 10^{-4}$ m

$$\frac{1}{k_d} = A \frac{(1-\varepsilon)^2}{\varepsilon^3 D_{\text{eq}}^2} \quad \beta = B \frac{1-\varepsilon}{\varepsilon^3 D_{\text{eq}}} \tag{10}$$

Channel and hole outlet pressure distributions are calculated by accumulating the losses due to friction, porous media, and through-hole flow:

$$P_{0,\text{ch}}(x) = P_{0,\text{ch}}(x - \Delta x) - \Delta P_{0,\text{fr}} - \Delta P_{0,\text{porous}},$$
$$P_{0,\text{eo}} = P_{0,\text{ch}} - \Delta P_{0,\text{eff}} \tag{11}$$

where porous media pressure drop is zero at the pressure side.

For all heat transfer calculations, Baehr and Stephan correlation is used (from p. 543 of Ref. [34]), together with the Sieder and Tate correction for variation in physical properties within each domain section (p. 369 in Ref. [35]), applicable when the wall is being cooled by the gas ($T_b < T_{\text{wall}}$):

$$\text{Nu}_{\text{base}}(\hat{u}, \hat{T}, \hat{P}, \hat{D}, \hat{x}, \widehat{T_b}) = \frac{(3.66/\tanh(2.264\text{Gz}_D^{-1/3} + 1.7\text{Gz}_D^{-2/3})) + 0.0499\text{Gz}_D \tanh(\text{Gz}_D^{-1})}{\tanh(2.432\,\text{Pr}^{1/6}\text{Gz}_D^{-1/6})}(\widehat{T_b}/T_{\text{Wall}})^{0.47} \tag{12}$$

$$\text{Gz}_D = (\hat{D}/\hat{x}) \cdot \text{Re} \cdot \text{Pr}, \quad \text{Re} = \frac{\hat{\rho} \cdot \hat{u} \cdot \hat{D}}{\hat{\mu}}$$

The Graetz number, Gz_D, in the expression accounts the non-fully developed nature of both the temperature and velocity profiles. Then, the convective heat flux and the accompanying coolant temperature rise can be calculated by

$$Q_{\text{base}}(\widehat{\text{Nu}}, \hat{A}, \widehat{T_b}) = \hat{h} \cdot \hat{A} \cdot (T_{\text{Wall}} - \widehat{T_b}), \quad \Delta T_{\text{base}}(\hat{Q}, \hat{m}) = \frac{\hat{Q}}{\hat{m}c_p} \tag{13}$$

The equation set described in Eqs. (12) and (13) are applied to all the three control volumes CV_1–CV_3 to quantify the convective heat transfer in each domain. The subscript "base" is used because it will be modified for CV_2 in Eq. (17) to take into account the presence of the holes (i.e., shed vortices and streamline curvature). Here, T_{wall} is a general expression and applies to respective walls, which is $T_{w\text{-in}}$ for the internal channel (CV_1–CV_2) and $(T_w + T_{w\text{-in}})/2$ for CV_3.

The heat transfer evaluation starts from the part of the internal channel flow that is locally unaffected from hole suction (CV_1):

$$\text{Nu}_{CV_1} = \text{Nu}_{\text{base}}(\overline{u_{\text{ch}}}, T_{\text{ch}}, P_{\text{ch}}, D_{\text{hyd}}, x, T_{\text{ch}}) \tag{14}$$

where the Reynolds number (Re) is calculated based on streamwise average channel velocity $\overline{u_{\text{ch}}}$ (from the inlet of the considered sector) and hydraulic diameter D_{hyd}. The streamwise parameter x_0 is defined as the curve-linear location from the leading edge, x. The density and viscosity are estimated according to local quantities, determined by the local temperature and pressure, $T_{\text{ch}}(x)$ and $P_{\text{ch}}(x)$. From Eq. (13), the extracted heat Q_1 and temperature rise

in every sector ΔT_1 are

$$Q_{CV_1} = Q_{\text{base}}\left(\text{Nu}_{CV_1}, \frac{1}{5}\text{pit} \cdot \text{pit}, T_{\text{ch}}\right)$$
$$\Delta T_{CV_1} = \Delta T_{\text{base}}(Q_{CV_1}, \dot{m}_{\text{ch}}(x) - \dot{m}_{\text{eff}}(x)) \tag{15}$$

Since CV_1 accounts for channel flow region that is unaffected by hole suction, the hole through flowrate is excluded from the mass flow operating in this control volume, and effective area is assumed to be 1/5 of the shell internal area (which is the square of pitch). This empirically obtained area fraction indicates that most of the heat that enters the internal channel in a certain sector (through a total area of pit2) exits with the ejected mass from the hole. Then, the local channel temperature $T_{\text{ch}}(x)$ can be calculated as

$$T_{\text{ch}}(x) = T_{\text{ch}}(x - \Delta x) + \Delta T_{CV_1} \tag{16}$$

Indicated by CV_2 in Fig. 3, the heat transfer is calculated for the portion of the internal channel flow locally being sucked into the neighboring hole as

$$\text{Nu}_{CV_2} = \text{Nu}_{\text{base}}\left(u_{\text{ch}}, T_{\text{ch}}, P_{\text{ch}}, \text{pit}, \text{pit}, \frac{T_{\text{ch}} + T_{\text{ei}}}{2}\right)$$
$$\cdot (1 + c \cdot (\text{pit}/D)^{-n}) \tag{17}$$

In order to account for the heat transfer ramifications of streamline curvature associated with flow turning to enter into the hole and vortex shedding from the upstream hole, an additional correction factor is included in the correlation (see Eq. (17)), where the constants are $c = 2.01$ and $n = 0.4$, consistent with a 90 deg sharp edge case (p. 363 from Ref. [35]). In the equation, the velocity

and channel flow properties are calculated based on channel local values. The characteristic length scale associated with Reynolds number and the streamwise position are both taken as hole pitch (rather than the diameter and the absolute x position, see Eq. (12)), which would imply that the heat transfer is considered for conditions where the CV_2 domain boundary layer is fully purged and restarts after each hole. Therefore, in CV_1, the heat transfer grows cumulatively from the start; but in CV_2, it resets after each hole. Furthermore, the bulk temperature in CV_2 is considered to be an average between the internal channel temperature (the common inlet with CV_1) and hole inlet (outlet of CV_2) temperatures.

Then, the net heat flux and temperature rise in CV_2 can be computed as

$$Q_{CV_2} = Q_{base}\left(Nu_{CV_2}, \frac{4}{5} pit \cdot pit - \frac{\pi D^2}{4}, \frac{T_{ch} + T_{ei}}{2}\right)$$

$$\Delta T_{CV_2} = \Delta T_{base}(Q_{CV_2}, \dot{m}_{eff}) \tag{18}$$

The area is the remainder shell surface not covered by CV_1, and the bulk temperature is taken as the average of the local channel and hole inlet temperatures. For most of the domain, the effective mass flowrate that CV_2 encompasses is considered to be limited to the fluid entering the hole. However, in the plenum area, this is expanded to

$$\dot{m}_{eff} = K_{pl} \cdot \dot{m}_{eo} + (1 - K_{pl}) \cdot \dot{m}_{ch} \tag{19}$$

where K_{pl} is 0.96 at the leading edge point and 1 after the plenum ends (found empirically).

Then the temperature at the inlet of the hole T_{ei} can be computed as

$$T_{ei}(x) = T_{ch}(x) + \Delta T_{CV_2} \tag{20}$$

Lastly, hole outlet temperatures T_{eo} are calculated for CV_3, representing the through-hole flow regions:

$$Nu_{CV_3} = Nu_{base}\left(u_{eo}, \frac{T_{eo} + T_{ei}}{2}, \frac{P_{eo} + P_{ei}}{2}, D, d_s, T_{ei}\right)$$

$$Q_{CV_3} = Q_{base}(Nu_{CV_3}, \pi D \cdot d_s, T_{ei})$$

$$\Delta T_{CV_3} = \Delta T_{base}\left(Q_{CV_3}, m_{eff}, \frac{T_{eo} + T_{ei}}{2}\right)$$

$$T_{eo} = T_{ei} + \Delta T_{CV_3} \tag{21}$$

where Reynolds number is based on hole diameter, hole outlet velocity, and mid-section flow properties; streamwise parameter equals to hole length; and local bulk temperature is hole inlet temperature.

After the flow field is converged for a certain metal temperature, heat balance is applied on the shell, considering convective heat transfer from external side (Q_{ext}), internal channel side ($Q_{CV_1} + Q_{CV_2}$), and effusion holes (Q_{CV_3}), as well as conduction amongst neighboring metal segments (Q_m):

$$Q_{net} = Q_{ext} + Q_{CV_1} + Q_{CV_2} + Q_{CV_3} + Q_m$$

$$Q_m|_i = kA_{metal}\left(\left.\frac{dT_{w-avg}}{dx}\right|_+ + \left.\frac{dT_{w-avg}}{dx}\right|_-\right) \tag{22}$$

Next, the wall temperature is updated in every iteration using the net heat (unbalance), until Q_{net} converges to zero in steady state:

$$T_{w-avg}|_{k+1} = T_{w-avg}|_k + \frac{Q_{net}}{(\dot{m}c_p)_m} \tag{23}$$

Fourier heat conduction law is used to calculate the surface temperature (T_w) for a known external heat flux and the shell inner temperature (T_{w-in}) is extrapolated in the wall thickness direction linearly with known external and average temperatures:

$$T_w = T_{w-avg} + q'' \cdot \frac{0.5 d_s}{k}$$

$$T_{w-in} = T_w - 2 \cdot (T_w - T_{w-avg}) \tag{24}$$

where d_s is the shell metal thickness. Since both sides of the blade are solved separately, metal temperature of each side (leading and trailing edges) is used for obtaining metal temperature derivative equation (22), and thus the whole blade is solved as one. The uncooled trailing edge is another source of heat outside the calculation domain. Therefore, this heat source is modeled by enlarging the convective area of heat flux by 2 mm in SC3X case in the curvelinear direction: $Q_{ext} = q'' \cdot (A + pit \cdot 2 \cdot 10^{-3})$. Then, once the metal wall temperatures are updated, the flow field solution is iterated until convergence.

Effusion Cooling Module. With the updated metal temperature distribution, coolant mass flowrates, and outflow temperatures known from the conjugate heat transfer module (the first block in Fig. 1), the external heat flux load stemming from the convective heat transfer on the cooled turbine blade surface is updated by the effusion cooling module (the second block in Fig. 1).

Effectiveness formulation locally compares the deviation of the adiabatic wall temperature (T_{aw}) from the freestream (T_∞), with the deviation of the coolant exit temperature (T_{eo}) from the freestream:

$$\eta = \frac{T_\infty - T_{aw}}{T_\infty - T_{eo}} \tag{25}$$

which provides a measure of the coolant coverage along the blade surface of the blade.

At first, the lateral-averaged film cooling effectiveness is calculated for each hole separately, using a well-established flat plate correlation given in Ref. [4]:

$$\eta = \frac{1}{S + c_1 M^{c_2} \xi^{c_3}} \tag{26}$$

where S is the spacing parameter, M is the blowing ratio, and ξ is the normalized streamwise direction:

$$S = \frac{pit}{D}, \quad M = \frac{\rho_{eo} u_{eo}}{\rho_\infty u_\infty}, \quad \xi = \frac{x}{MS_e}, \quad S_e = \frac{\pi D^2/4}{pit}$$

where S_e is the equivalent slot width and the constants c_1, c_2, and c_3 are equal to 0.1721, -0.2664, 0.8749, respectively. It appears that the peak effectiveness is proportional to $1/S$, and therefore, spacing parameter has a large influence in the vicinity of the holes.

In order to capture the blade curvature impact on effectiveness, the experimental findings that tabulate film effectiveness augmentation (K_{curv}) with local normalized radius (r/D) as a function of momentum flux ratio (I) are utilized [36]. For concave surfaces with blowing ratio of ~1, it has been shown that curvature effects are negligible [37]. For convex surfaces, the experimental film effectiveness augmentation values of C3X blade are available for two curvature surfaces, and the surface is extrapolated for values below $2r/D < 290$. The resultant employed curvature correction factor K_{curv} is presented in Fig. 5. The updated curvature-corrected effectiveness can then be calculated locally as

$$\eta_{curv} = \eta K_{curv}\left(\frac{r}{D}, I\right)$$

$$\text{Convex:} \quad K_{curv} = K_{curv}\left(\frac{r}{D}, I\right) \tag{27}$$

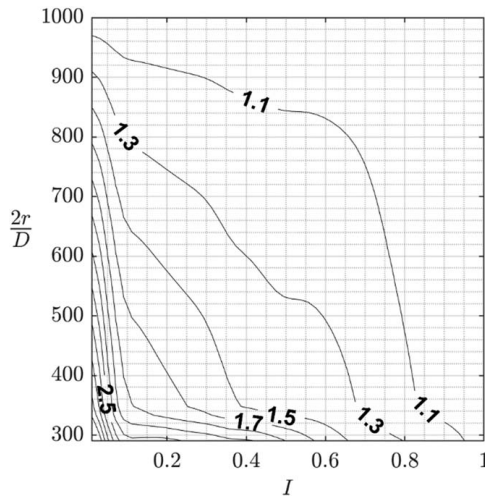$$\text{Concave:} \quad K_{curv} = 1$$

Fig. 5 Film effectiveness augmentation (K_{curv}) with respect to scaled curvature (r/D) and momentum flux ratio (I) on convex surfaces (reconstructed from Ref. [36])

Table 2 Parameters of hole exit static pressure distribution for Eq. (33)

	A1	A2	A3
C_1	−40,000	−16,000	−5333.3
C_2	406,000	404,000	401,333
C_3	250,000	280,000	320,000
x_1 mm	3.75	7.5	15

where D is the hole diameter, and r is the curvature radius calculated by

$$r = \frac{\left(X'^2 + Y'^2\right)^{3/2}}{|X'Y'' - Y'X''|} \qquad (28)$$

Then, the compound effectiveness which results from the coolant buildup in streamwise direction along the blade surface can be computed by the methodology described in Ref. [7]. For the reader's convenience, the final set of equations are repeated here below:
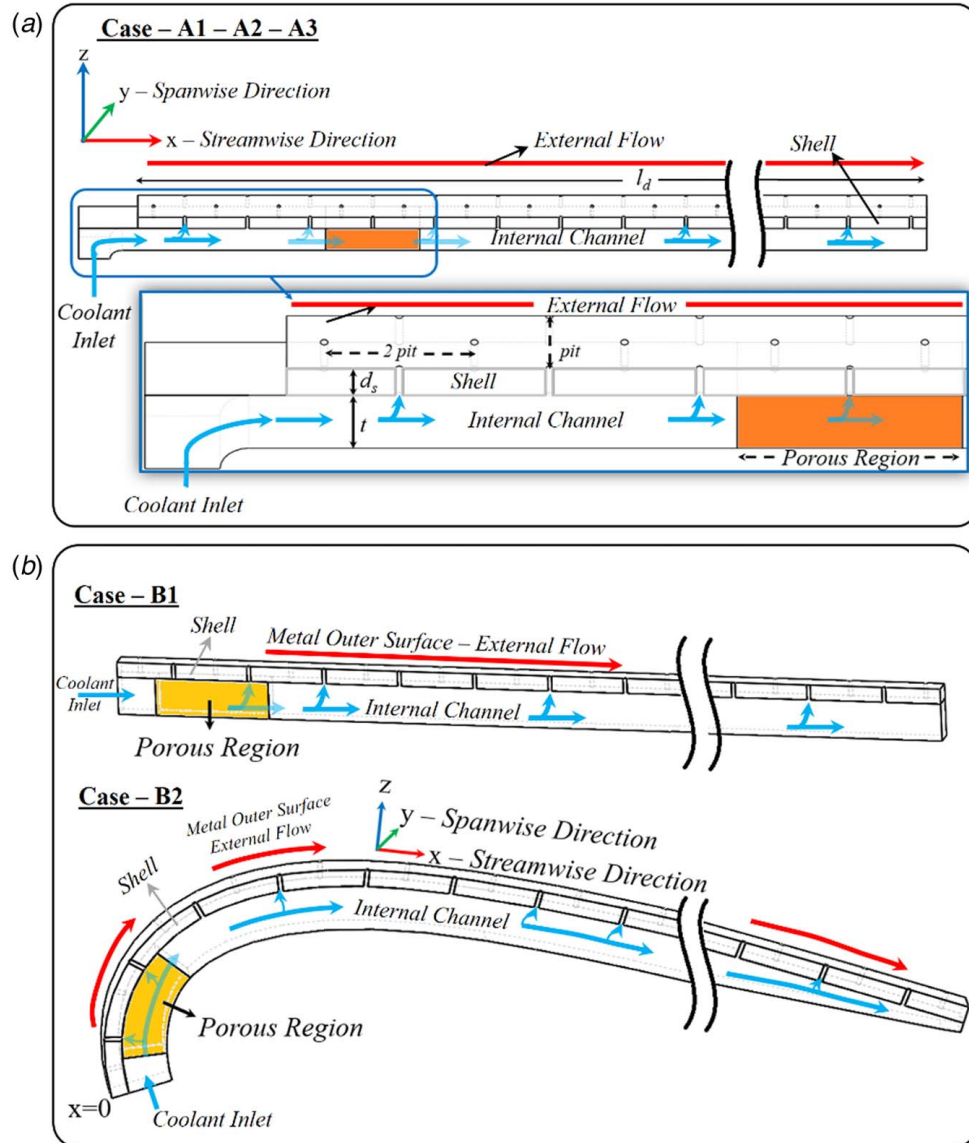

Fig. 6 Conjugate heat transfer module validation geometries with external shell outer wall subjected to isothermal boundary condition

$$m_{ei}(x) \equiv m_{ci}\left(\frac{1}{\eta_i(x)} - 1\right)$$

$$\frac{dm_{ei}(x)}{dx} = -\frac{m_{ci}}{\eta_i^2(x)}\frac{d\eta_i(x)}{dx}$$

$$T_{01}(X) = \begin{cases} \dfrac{T_{0c}m_{c1} + T_{0\infty}m_{e1}(X)}{m_{c1} + m_{e1}(X)}, & x_1 \leq X < x_2 \\[2ex] \dfrac{T_{0c}m_{c1} + T_{0\infty}m_{e1}(X) - \int_{x_2-\delta x}^{X} T_{01}(x)(dm_{e2}(x)/dx)dx}{m_{c1} + m_{e1}(X) - m_{e2}(X)}, & X \geq x_2 \end{cases}$$

$$T_{0i}(X) = \begin{cases} \dfrac{T_{0c}m_{ci} + \int_{x_i-\delta x}^{X} T_{0(i-1)}(x)(dm_{ei}(x)/dx)dx}{m_{c1} + m_{e1}(X)}, & x_i \leq X < x_{i+1} \\[2ex] \dfrac{T_{0c}m_{ci} + \int_{x_i-\delta x}^{X} T_{0(i-1)}(x)(dm_{ei}(x)/dx)dx - \int_{x_{i+1}-\delta x}^{X} T_{0i}(x)(dm_{e(i+1)}(x)/dx)dx}{m_{ci} + m_{ei}(X) - m_{e(i+1)}(X)}, & X \geq x_{i+1} \end{cases}$$

$$T_{0n}(X) = \frac{T_{0c}m_{cn} + \int_{x_n-\delta x}^{X} T_{0(n-1)}(x)(dm_{ei}(x)/dx)dx}{m_{cn} + m_{en}(X)}, \quad X \geq x_n$$

(29)

Starting from the leading edge, local enthalpy is computed at every location in each layer of coolant, the entrainment mass flowrate of each film layer along the streamwise direction is considered, and enthalpy conservation between the adjacent layers is imposed. The input variables are cooling effectiveness from Eqs. (26) and (27), hole exit total temperatures and coolant mass flowrates from the CHT module. The output is the local effectiveness values.

At this stage, in order to calculate the local external heat flux distribution, the only remaining unknown is the heat transfer coefficient on the external surface of the cooled turbine blade. This can be estimated through augmentation of the uncooled adiabatic heat transfer coefficient (h_0) (input to the reduced order model) by coolant-mainstream mixing. Inspired by the correlation in Ref. [38] for a single row of film cooling holes, the following relation is used to model the compound effusion-cooled blade adiabatic heat transfer coefficient:

$$h_f/h_0 = [1 - 500\,\text{K}] \cdot [1 + \eta] \cdot \left[1 + 1.11\, M_\theta \exp\left(-0.14\, \frac{x}{D}M_\theta^{-1}\right)\right]$$
(30)

Two parameters are taken from the original correlation: the streamwise coordinate normalized by hole diameter (x/D) and acceleration factor ($K = \nu/U_\infty(du_\infty/dx)$). The streamwise coordinate affects the single hole augmentation decay rate. The blowing ratio, which influences the decay rate as well, is taken from the original correlation with a minor additional adjustment for the injection angle (ϕ), calculated relative to the local mainstream, resulting in $M_\theta = \rho_{eo}u_{eo}\sin(\phi)/\rho_\infty u_\infty$. The acceleration factor lessens the augmented heat transfer coefficient by up to 25%, mostly in the leading edge, where there is strong favorable pressure gradient [38].

Two additional correction parameters are introduced in Eq. (30) in order to capture the increase in HTC associated with a local rise in turbulence intensity. The first is employing the adjusted blowing ratio M_θ to model HTC augmentation amplitude (by multiplying it with the exponential term). As blowing ratio increases, more turbulence intensity is generated due to jet and mainstream interaction. The second is utilizing effectiveness (η) to capture the compound effect of multiple cooling holes and the associated accumulation of turbulent coherent structures.

Using lateral-averaged adiabatic cooling effectiveness η, cooling augmented HTC h_f, and normalized coolant temperature θ, the freestream-referenced heat transfer coefficient can be computed from

$$h = h_f(1 - \eta\theta)$$
(31)

where $\theta = (T_\infty - T_{eo})/(T_\infty - T_w)$.

With this estimated freestream-referenced heat transfer coefficient in the presence of cooling and the recovery temperature T_∞, the heat flux on the blade surface can be calculated as

$$q'' = h(T_w - T_\infty)$$
(32)

for each metal temperature T_w, resulting from the CHT calculations. Convergence of the reduced order model is achieved by obtaining the wall temperature from the CHT module and iterating over the heat flux from the EC module, while applying under-relaxation factors.

An example of the under-relaxation factor implementation is described by $T_k = urf \cdot T_k^* + (1 - urf) \cdot T_{k-1}$. While the rest of the under-relaxation factors are constant, in this case the urf value starts at 0.8 in the first iterations and decreases exponentially according to $urf = 0.8 \cdot \exp(-0.1 \cdot k)$, until it reaches $urf \cong 0.3$. T_k is the current iteration wall temperature distribution, T_k^* is the wall temperature distribution in current iteration before applying urf modification, and T_{k-1} is the wall temperature distribution in previous iteration. The urf is used for evaluating the error in each iteration: $\text{err}(T_k) = 1/urf \cdot \max(|(T_k - T_{k-1})/T_k|) \cdot 100$. The under-relaxation factor enables general robustness in the code, particularly in geometries with higher temperature gradient, where convergence time may be longer.

Validation of Reduced Order Model

In order to ensure that the reduced order model represents the highly coupled complex physics, the conjugate heat transfer module is compared to 3D CFD, absent of external flow. Then, experimental validation is conducted on available flat plate data for film cooling effectiveness in the absence and presence of conduction and internal flow.

Conjugate Heat Transfer Module Validation. Comprising the first step of the reduced order model, the conjugate heat transfer module is compared to 3D CFD of several internal channels, where effusion cooling shell structure constitutes one of the side walls (Fig. 6). The coolant inlet total pressure and temperature ($P_{0,\text{in}}$ and $T_{0,\text{in}}$) are specified for each simulation. A porous media is placed in an intermediate location along the internal channel as a local blockage mechanism, preventing blow off further downstream (typically at the suction side due to lower hole discharge pressures relative to the pressure side). For the one pitch deep domain, the lateral surfaces (out of plane in Fig. 6) are simulated as symmetric. The interior wall of the core is adiabatic, and the external outer wall of the shell is subjected to isothermal boundary condition.

As established and validated previously, ANSYS FLUENT 19.1 is used to solve both the fluid and the conduction in the solid domains. The k–ε realizable model with Menter Lechner near-wall treatment (ML-ε) is used for turbulence closure. The aerodynamic characteristics of the porous region are captured by viscous permeability and inertial resistance, which are taken as the same values used for the ROM. Based on mesh independency study, the maximum element size is 0.01 mm, resulting in 4.3 M elements. Two basic geometric variations are considered based on the general features of the C3X geometry scaled down to 23.1% of its original size, which results in blade chord length of 33.5 mm.

Parametric variation A focuses on the impact of differing uniform hole pitch over diameter ratios 5, 10, and 20 for cases A1, A2, and A3, respectively. Exit of each hole on the shell structure is subjected to a value of static pressure ($P_{s,\text{eo}}$) linearly decreasing from the inlet until a given x_1 position and constant downstream of it

$$P_{0,\text{eo}}(x) = C_1 x + C_2 \quad \text{if } x \leq x_1$$
$$P_{0,\text{eo}}(x) = C_3 \quad \text{if } x > x_1 \tag{33}$$

where the parameters are specified in Table 2.

Ensuring the validation results are not boundary condition dependent, parametric variation B diversifies the solutions by changing the inlet/exit flow conditions, and metal shell properties for a constant hole pitch over diameter 10. In this case, the boundary conditions are inspired by the NASA report [39], and the hole exit static pressure distribution is identical to the suction side of C3X under the conditions of experimental run 158 [39]. Furthermore, the impact of internal channel flow path curvature is captured by comparing B1 and B2; the latter being the suction side of scaled-C3X geometry. The details of the domain for each configuration are summarized in Table 3.

In order to assess the zero-order performance of the reduced order model for several hole pitch configurations considered in variations A, the ROM is compared to the CFD in Fig. 7. Several 1D metrics are used for the purpose: the hole exit velocity that captures the external coolant coverage performance, the hole exit pressure and temperature normalized by their respective coolant supply values, which relate to the through-flow aerodynamic and heat transfer performance, respectively, and the local hole mass flowrate that infers information about the utilized coolant consumption. The velocity is computed by area weighted averaging while the temperature and pressure are computed by mass weighted averaging. Comparing the predictions of the conjugate heat transfer module with respect to 3D CFD, an excellent agreement is observed. The only locations with noticeable local deviations are at the porous media regions, positioned at x/arc equals to 0.094, 0.187, and 0.375 for pitch to diameter ratios of 5, 10, and 20, respectively. This is considered to be associated with the local sudden change in flow regime. The main
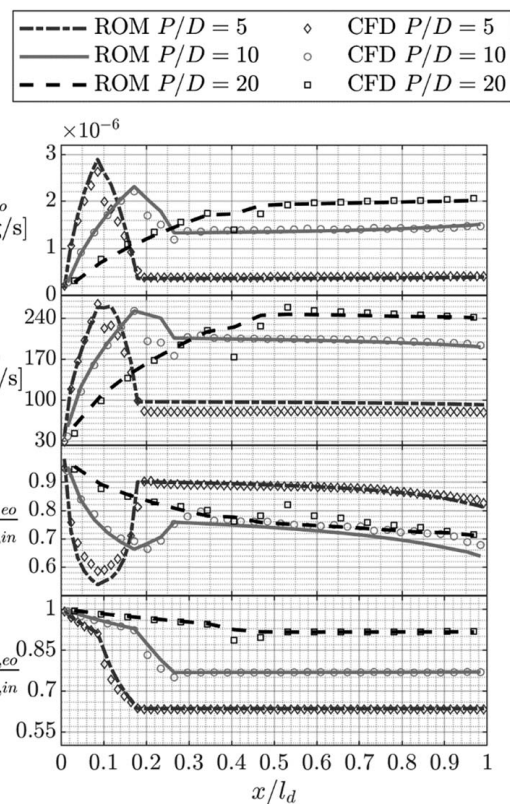

Fig. 7 Comparison between reduced order model and CFD for hole pitch variations—cases A1, A2, and A3 in Table 3

driving mechanisms of the flow inside the internal channel and effusion holes are channel Reynolds number and pressure ratio. The behavior of mass flowrate, velocity, and temperature are due to low static to total pressure ratio. As velocity increases rapidly right after the coolant inlet, Reynolds number increases, Graetz number increases, and the heat transfer through the holes decreases. In addition, effusion outlet temperature gradually decreases in the streamwise direction due to ejection from the internal channel, where Reynolds number decreases, Graetz number decreases, and therefore heat transfer coefficient decreases as well.

Considering a different set of geometric conditions with more complex boundary conditions, Fig. 8 presents the hole exit aerothermal flow characteristics in data set associated with variations B. Excellent agreement is observed comparing the findings with CFD both for the straight and curved internal channel flow paths.

Towards quantitatively estimating the accuracy of the conjugate heat transfer module, the average deviations from CFD results are summarized in Table 4. The deviations are generally less than 5%, except case A1 (Pit/$D = 5$) where the mean magnitude of mass flowrates and velocities are small "per hole." As the pitch-to-diameter ratio decreases below 5, the physics deviate further away from a distinct internal channel with a cooling hole and tend towards porous media-like aerodynamic behavior, not modeled in the present study. Therefore, pit/$D = 5$ is considered as the lower limit on the parameter space.

Modeling quasi-2D conduction in the shell has a major impact on ROM accuracy. The film effectiveness and hole discharge temperature distributions for two different thermal conductivity values, $k = 1$ and 30 W/mK (nominal $k = 18$ W/mK), are compared on the B2 case. Expectedly, the wall temperature exhibits sharper gradients when there is no conduction, with local deviations up to 50 K. The hole mass flowrate and the blowing ratio are not significantly affected. However, with reduced conduction, it is found that effectiveness increases on average by 5% with local deviations up to 10%. In terms of hole discharge temperature, the maximum difference can be as high as 30 K. Therefore, the quasi-2D modeling,

Table 3 Principal parameters for the internal cooling validation test model

|	A1–A3	B1–B2
Domain length, l_d (mm)	32	33
Number of holes	64, 32, 16	33
Pitch over diameter, S	5, 10, 20	10
Porous normalized position	0.094, 0.187, 0.375	0.03
Porous length (mm)	3	3, 2.3
Diameter of the holes, D (mm)	0.1	0.1
Blade shell thickness, ds (mm)	0.5	0.4
Flow channel thickness, t (mm)	1	1
Coolant inlet total pressure (kPa)	400	246
Coolant inlet total temperature (K)	400	383
Outer wall temperature (K)	1200	600
Shell density (kg m^{-3})	8908	7900
Shell heat capacity (J kg^{-1} K^{-1})	502	586
Shell conductivity (W m^{-1} K^{-1})	91	18
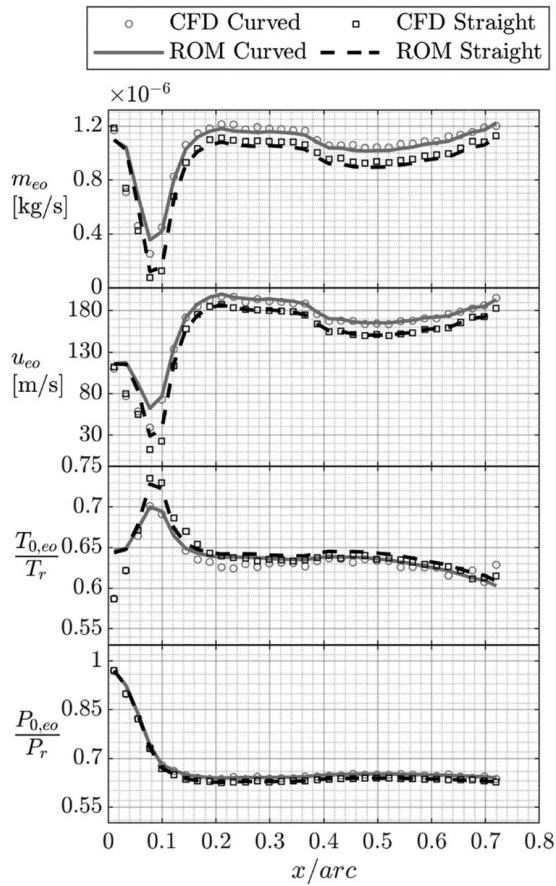
Fig. 8 Comparison between reduced order method and CFD for straight and curved channels with complex boundary conditions —cases B1 and B2 in Table 3

both in streamwise and wall-normal, is an important feature of the reduced order framework.

Experimental Film Effectiveness Validations. As the final step of validation, the output of the reduced order model is compared to the experimental flat plate film cooling effectiveness data from the literature. The experiment conducted by Krawciw et al. [40] consists of a configuration where the coolant is fed by a plenum (not through an internal channel) and presents an opportunity to assess the performance of effusion cooling in an isolated setting. The cooled plate surface consists of 30 deg-slanted and 3-mm-diameter 9×5 staggered effusion holes drilled at a pitch-to-diameter ratio of 5.

Tested using pressure sensitive paint (PSP), Fig. 9 presents adiabatic effectiveness distribution at blowing ratios of $M = 0.8$ and 1.5. Both the ROM and the experiments show a similar trend: adiabatic film effectiveness ($\eta_{\text{adiabatic}}$) is initially lower for $M = 1.5$ relative to $M = 0.8$ until roughly around $x/D = 4$. For $x/D > 4$, the reverse occurs and $M = 1.5$ starts to have higher effectiveness. However, ROM under predicts $\eta_{\text{adiabatic}}$ at $x/D < 4$. The maximum error

Table 4 Average deviation of conjugate heat transfer module from CFD for different validation cases

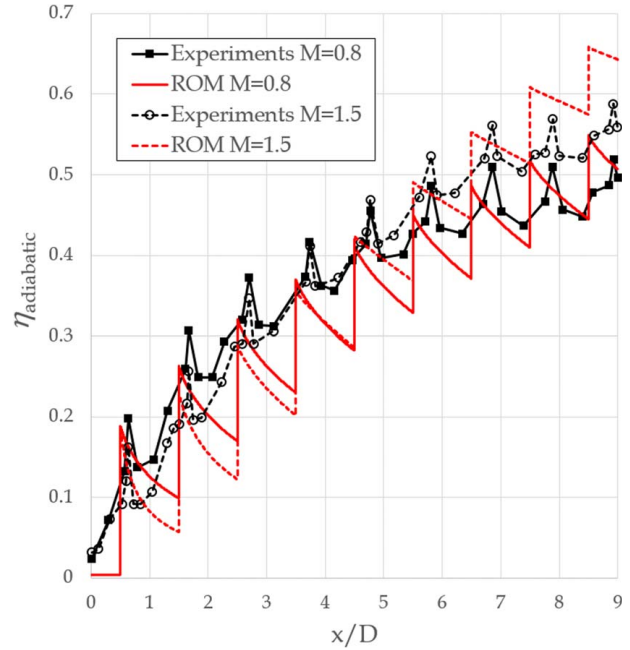| Case	$\dot{m}_{\text{eo}}$ (%Err)	u_{eo} (%Err)	$T_{0,\text{eo}}$ (%Err)	$P_{0,\text{eo}}$ (%Err)
A1	10.8	15.1	1.5	0.8
A2	3.6	3.3	3.3	0.5
A3	4.2	4.3	2.4	0.5
B1	4.9	2.4	1.2	0.5
B2	4.2	2.8	1.3	0.3

Fig. 9 Comparison of laterally averaged effectiveness η between ROM and experiments [40]

(averaged around each hole) reaches up to 32% for the first hole, while the averaged error for the whole case is around 11%. Apart from the 22% uncertainty of the PSP data, the low number of holes (stronger end-effects) and the presence of a plenum supply rather than an internal channel, for which the ROM is developed, may have contributed to this discrepancy. Moreover, $\text{pit}/D = 5$ is shown to be the lower limit of the parameter space of the ROM.

In another experimental study, Qu et al. [24] assessed the effectiveness of effusion cooling, in the presence of internal flows and metal conduction effects. (Although this study concentrates on combined slot and effusion cooling, pure effusion data are also presented.) The 30×15 30 deg-inclined holes are staggered along a 180×90 mm flat plate; the hole diameter is 1 mm and pitch is $6D$. The stainless steel plate has a thermal conductivity and thickness of 26 W/m^2 K, 1 mm, respectively, whereas the adjacent internal channel has a height of 30 mm. The considered experimental conditions for mainstream and coolant temperatures are 700 K and 298 K. In addition to the external flow, the internal duct parallel to the effusion plate and the resultant non-uniform hole flowrate
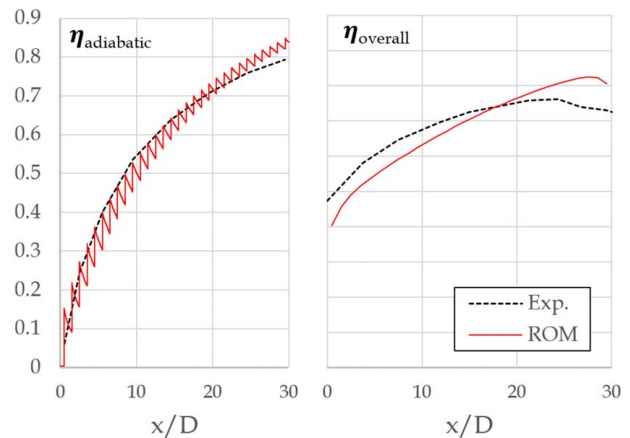

Fig. 10 Comparison of laterally averaged adiabatic (left) and overall (right) effectiveness η between ROM and experiments at average $M = 1.2$ [24]

distribution, and the conduction in the cooled plate bears significant resemblance to the conditions considered for the current problem.

Figure 10 presents the adiabatic and overall effectiveness results for average blowing ratio of $M = 1.2$. Overall effectiveness ($\eta_{overall}$) is defined in a similar manner with the adiabatic effectiveness, but the metal conduction is taken into account and the physical temperature (rather than the adiabatic temperature) distribution is considered at the wall. Comparing the output of the ROM with the experimental data, adiabatic film cooling effectiveness appears slightly under predicted, with 10% and 24% average and maximum errors, respectively (expected for pit/$D = 6$). However, the trends over the 30 streamwise holes are very well captured. When the conduction effects are also considered, it appears that overall cooling effectiveness is also well represented. The limited discrepancy is hypothesized to be an artifact of ambiguity in longitudinal solid boundary conditions in the experiment, including metal segments of unknown dimension upstream and downstream of the effusion plate.

Summary and Conclusions

A reduced order model is developed for single-wall effusion cooling in scope of gas turbine airfoil thermal management applications. It is assumed that the coolant is fed around the leading edge and flows towards the trailing edge in the internal channel while seeping through the holes that provide external cooling coverage from the outer hot gas path. The conjugate heat transfer module captures the physics of the internal flow between the inner core and the outer shell considering momentum-thermal boundary layers and quasi-2D (streamwise and wall-normal) shell conduction. The effusion cooling module evaluates compound effectiveness using existing film cooling correlations and enthalpy balance between layers of injected coolant propagating from upstream.

The conjugate heat transfer module is compared to 3D CFD absent of external flow. The parameters such as total pressure, total temperature, velocity, and mass flow at the holes match well within 5% except the pitch-to-diameter ratio of 5, where the mass flow and velocity errors rise up to 11% and 15%, respectively. Therefore, it is concluded that pit/$D = 5$ is considered as the lower limit on the parameter space, where smaller values resemble physics similar to porous media. Then, the adiabatic film cooling effectiveness is validated against experimental findings from a plenum-fed perforated surface. In this case, even if pit/$D = 5$, the averaged error between the predictions and the experiments is 11%. The maximum error (averaged around each hole) reaches to its peak value of 32% for the first hole. Apart from the experimental uncertainty of 22% and low pit/D, the low number of holes (just nine holes in streamwise, stronger end-effects) and the presence of a plenum supply rather than an internal channel (for which the ROM is originally developed) may have contributed to this discrepancy. However, the trends are well captured, including the relative effectiveness behaviors of two blowing ratios ($M = 0.8$ and 1.5). Lastly, the predictions of the ROM are compared with an experiment that consists of internal flow over a perforated flat plate that provides external coolant coverage. In this case, the average and maximum errors are around 10% and 24%, respectively, which are expected for pit/$D = 6$. Again, the trends are well captured.

In conclusion, the developed methodology is observed to predict the complex physics of single-wall effusion cooling reasonably well. In Part II, further CFD validation of fixed hole diameter and pitch case is presented on a small turbine airfoil geometry with strong external curvature; later, the main utility of this low fidelity model as a preliminary design tool is highlighted through integration into an optimization framework.

Acknowledgment

Conflict of Interest

There are no conflicts of interest.

Data Availability Statement

The datasets generated and supporting the findings of this article are obtainable from the corresponding author upon reasonable request.

Nomenclature

c = blade chord length (mm)
f = friction factor
h = convection coefficient (W m^{-2} K^{-2})
k = conduction coefficient (W m^{-1} K^{-1})
$\dot{m}$ = mass flowrate (kg s^{-1})
r = local curvature radius (mm)
t = thickness (mm)
u = velocity (m s^{-1})
x = curve-linear or streamwise direction (mm)
y = span wise direction (mm)
z = direction normal to the blade (mm)
A = surface wetted area (m^2)
D = effusion hole diameter (μm)
I = momentum flux
K = acceleration factor
L = hole length (mm)
M = blowing ratio or Mach number
P = density ratio
Q = rate of heat transfer (W)
R = specific ideal gas constant (J kg^{-1} K^{-1})
S = spacing parameter (pitch/diameter)
T = temperature (K)
V = velocity ratio
d_s = shell thickness (mm)
k_d = Darcy's permeability factor (m^2)
k_v = viscous correction coefficient
l_d = domain length (mm)
A_{act} = effective hole area (m^2)
C_D = discharge coefficient
C_p = specific heat capacity (J kg^{-1} K^{-1})
D_{eq} = mean sphere diameter (mm)
D_{hyd} = hydraulic diameter (mm)
K_{CD} = conversion factor from loss to discharge coefficient
K_{pl} = plenum correction
K_T = minor loss coefficient
K_{curv} = curvature correction factor
S_e = equivalent slot width (mm)
T_U = turbulence intensity
q'' = heat flux (W m^{-2})
pit = hole's pitch (mm)
urf = under-relaxation factor
Nu = Nusselt number
Pr = Prandtl number
Re = Reynolds number
Gz_D = Graetz number
β = inertial resistance (m^{-1})
γ = specific heat ratio
ΔP = pressure loss (Pa)
$\delta^\star$ = displacement thickness (mm)
ε = friction coefficient
η = lateral-averaged adiabatic cooling effectiveness
θ = normalized coolant temperature
ν = kinematic viscosity (m^2 s^{-1})
ϕ = injection angle in degrees

Subscripts and Superscripts

0 = no cooling/stagnation conditions
1 = mainstream inlet

2 = mainstream outlet
aw = adiabatic wall
b = bulk
c = coolant
ch = internal channel
ei = effusion holes inlet
eo = effusion holes outlet
ext = external
eff = effusion holes
f = with cooling
fr = friction
i = inlet
m = metal
Porous = porous media
ps = pressure side
r = reference value
s = static conditions
ss = suction side
t = stagnation conditions
$w-$avg = center of each metal (shell) segment
w = outer shell (vane/blade) surface
w-in = inner shell surface
∞ = mainstream
$+$ = streamwise positive side
$-$ = streamwise negative side
$\blacksquare\char94$ = general variable

Abbreviations

CHT = conjugate heat transfer
CFD = computational fluid dynamics
CV = control volume
EC = effusion cooling
HTC = heat transfer coefficient
ROM = reduced order model
SC3X = scaled down C3X blade

References

[1] L'ecuyer, M. R., and Soechting, F. O., 1985, "A Model for Correlating Flat Plate Film Cooling Effectiveness for Rows of Round Holes," AGARD Heat Transfer and Cooling in Gas Turbines No. 12.

[2] Stone, L. D., and Goldstein, R. J., 1994, "Film Cooling Effectiveness Data for Simple Injection," Int. J. Rotating Mach., **1**(1), pp. 73–81.

[3] Boyle, R. J., and Ameri, A. A., 2010, "A Correlation Approach to Predicting Film Cooled Turbine Vane Heat Transfer," Proceedings of the ASME Turbo Expo 2010: Power for Land, Sea, and Air. Volume 4: Heat Transfer, Parts A and B, Glasgow, UK, June 14–18, pp. 1841–1856.

[4] Colban, W. F., Thole, K. A., and Bogard, D., 2011, "A Film-Cooling Correlation for Shaped Holes on a Flat-Plate Surface," ASME J. Turbomach., **133**(1), p. 011002.

[5] Chowdhury, N. H. K., Zirakzadeh, H., and Han, J. C., 2017, "A Predictive Model for Preliminary Gas Turbine Blade Cooling Analysis," ASME J. Turbomach., **139**(9), p. 091010.

[6] Sellers, J. P., 1963, "Gaseous Film Cooling With Multiple Injection Stations," AIAA J., **1**(9), pp. 2154–2156.

[7] Kirollos, B., and Povey, T., 2015, "An Energy-Based Method for Predicting the Additive Effect of Multiple Film Cooling Rows," ASME J. Eng. Gas Turbines Power, **137**(12), p. 122607.

[8] Fuqua, M. N., and Rutledge, J. L., 2021, "Film Cooling Superposition Theory for Multiple Rows of Cooling Holes With Multiple Coolant Temperatures," ASME J. Turbomach., **143**(11), p. 111003.

[9] Eriksen, V. L., and Goldstein, R. J., 1974, "Heat Transfer and Film Cooling Following Injection Through Inclined Circular Tubes," ASME Paper 74-HT-V, pp. 239–245.

[10] Hodges, J., 2015, "A Full Coverage Film Cooling Study: The Effect of an Alternating Compound Angle," M.Sc. thesis, University of Central Florida, Orlando, FL.

[11] Andrews, G. E., and Mkpadi, M. C., 1984, "Full-Coverage Discrete Hole Wall Cooling: Discharge Coefficients," ASME J. Eng. Gas Turbines Power, **106**(1), pp. 183–192.

[12] Byerley, A. R., 1989, "Heat Transfer Near the Entrance to a Film Cooling Hole in a Gas Turbine Blade," Ph.D. dissertation, University of Oxford, Oxford, UK.

[13] Cukurel, B., Selcan, C., and Arts, T., 2012, "Film Cooling Extraction Effects on the Aero-Thermal Characteristics of Rib Roughened Cooling Channel Flow," ASME J. Turbomach., **135**(2), p. 021016.

[14] Scheepers, G., and Morris, R. M., 2009, "Experimental Study of Heat Transfer Augmentation Near the Entrance to a Film Cooling Hole in a Turbine Blade Cooling Passage," ASME J. Turbomach., **131**(4), p. 044501.

[15] Moon, H., Kim, K. M., Jeon, Y. H., Shin, S., Park, J. S., and Cho, H. H., 2015, "Effect of Thermal Stress on Creep Lifetime for a Gas Turbine Combustion Liner," Eng. Fail. Anal., **47**(A), pp. 34–40.

[16] National Research Council (U.S.), 1996, *Coatings for High-Temperature Structural Materials: Trends and Opportunities*, National Academy Press, Washington, DC.

[17] Karaoglanli, A. C., Doleker, K. M., and Ozgurluk, Y., 2017, "State of the Art Thermal Barrier Coating (TBC) Materials and TBC Failure Mechanisms," Adv. Struct. Mater., **33**, pp. 441–452.

[18] Martena, M., Botto, D., Fino, P., Sabbadini, S., Gola, M. M., and Badini, C., 2006, "Modelling of TBC System Failure: Stress Distribution as a Function of TGO Thickness and Thermal Expansion Mismatch," Eng. Fail. Anal., **13**(3), pp. 409–426.

[19] Bunker, R. S., 2013, "Gas Turbine Cooling: Moving From Macro to Micro Cooling," Proceedings of the ASME Turbo Expo 2013: Turbine Technical Conference and Exposition. Volume 3C: Heat Transfer, San Antonio, TX, June 3–7, pp. 1–17.

[20] Krewinkel, R., 2013, "A Review of Gas Turbine Effusion Cooling Studies," Int. J. Heat Mass Transfer, **66**, pp. 706–722.

[21] Arcangeli, L., Facchini, B., Surace, M., and Tarchi, L., 2008, "Correlative Analysis of Effusion Cooling Systems," ASME J. Turbomach., **130**(1), pp. 1–7.

[22] Yang, L., and Rao, Y., 2019, "Predicting the Adiabatic Effectiveness of Effusion Cooling by the Convolution Modeling Method," Proceedings of the ASME Turbo Expo 2019: Turbomachinery Technical Conference and Exposition, Volume 5A: Heat Transfer, Phoenix, AZ, June 17–21, pp. 1–9.

[23] Gottiparthi, K. C., Cao, C., and Sankaran, V., 2019, "Modeling Effusion Cooling and Conjugate Heat Transfer Using Local Source Method," Proceedings of the ASME Turbo Expo 2019: Turbomachinery Technical Conference and Exposition. Volume 5B: Heat Transfer, Phoenix, AZ, June 17–21, pp. 1–12.

[24] Qu, L.-H., Zhang, J.-Z., and Tan, X.-M., 2017, "Improvement on Film Cooling Effectiveness by a Combined Slot-Effusion Scheme," Appl. Therm. Eng., **126**, pp. 379–392.

[25] Murray, A. V., Ireland, P. T., and Romero, E., 2019, "Experimental and Computational Methods for the Evaluation of Double-Wall, Effusion Cooling Systems," Proceedings of the ASME Turbo Expo 2019: Turbomachinery Technical Conference and Exposition. Volume 5A: Heat Transfer, Phoenix, AZ, June 17–21, pp. 1–16.

[26] Murray, A. V., Ireland, P. T., and Romero, E., 2020, "An Experimentally Validated Low Order Model of the Thermal Response of Double-Wall Effusion Cooling Systems for HP Turbine Blades," Proceedings of the ASME Turbo Expo 2020: Turbomachinery Technical Conference and Exposition. Volume 7A: Heat Transfer, Virtual, Sept. 21–25, pp. 1–13.

[27] Blasius, H., 1908, "The Boundary Layers in Fluids With Little Friction," Math. Phys., **56**(1), pp. 1–37.

[28] Humpherys, A. S., 1987, "Energy Dissipation in Low Pressure Irrigation Pipelines: II Orifices," Trans. ASAE, **30**(1), pp. 0176–0182.

[29] Haaland, S. E., 1983, "Simple and Explicit Formulas for the Friction Factor in Turbulent Pipe Flow," ASME J. Fluids Eng., **105**(1), pp. 89–90.

[30] Gamil, A. A. A., Nikolaidis, T., Teixeira, J. A., Madani, S. H., and Izadi, A., 2022, "Assessment of Surface Roughness Effects on Micro Axial Turbines," Proceedings of the ASME Turbo Expo 2020: Turbomachinery Technical Conference and Exposition, Virtual, Sept. 21–25, 2020, pp. 1–11.

[31] Xia, M., Gu, D., Yu, G., Dai, D., Chen, H., and Shi, Q., 2016, "Influence of Hatch Spacing on Heat and Mass Transfer, Thermodynamics and Laser Processability During Additive Manufacturing of Inconel 718 Alloy," Int. J. Mach. Tools Manuf., **109**, pp. 147–157.

[32] Talebi, S. S., and Tousi, A. M., 2017, "The Effects of Compressor Blade Roughness on the Steady State Performance of Micro-Turbines," Appl. Therm. Eng., **115**, pp. 517–527.

[33] Macdonald, I. F., El-Sayed, M. S., Mow, K., and Dullien, F. A. L., 1979, "Flow Through Porous Media—The Ergun Equation Revisited," Ind. Eng. Chem. Fundam., **18**(3), pp. 199–208.

[34] Bergman, T. L., Lavine, A. S., Incropera, F. P., and Dewitt, D. P., 2011, *Fundamentals of Heat and Mass Transfer*, 7th ed., John Wiley & Sons, Jefferson City, MO.

[35] Lienhard, J. H., and Lienhard, J. H. V., 1981, *A Heat Transfer Textbook*, Institute of Technology Press, Cambridge, MA.

[36] Winka, J. R., Anderson, J. B., Boyd, E. J., Bogard, D. G., and Crawford, M. E., 2014, "Convex Curvature Effects on Film Cooling Adiabatic Effectiveness," ASME J. Turbomach., **136**(6), p. 061015.

[37] Schwarz, S. G., and Eckert, E. R. G., 1990, "The Influence of Curvature on Film Cooling Performance," ASME J. Turbomach., **113**(3), pp. 472–478.

[38] Ammari, H. D., Hay, N., and Lampard, D., 1991, "Effect of Acceleration on the Heat Transfer Coefficient on a Film-Cooled Surface," ASME J. Turbomach., **113**(3), pp. 464–471.

[39] Hylton, L. D., Mihelc, M. S., Turner, E. R., Nealy, D. A., and York, R. E., 1983, "Analytical and Experimental Evaluation of the Heat Transfer Distribution Over the Surfaces of Turbine Vanes," NASA Report 19830020105.

[40] Krawciw, J., Martin, D., and Denman, P., 2015, "Measurement and Prediction of Adiabatic Film Effectiveness of Combustor Representative Effusion Arrays," Proceedings of the ASME Turbo Expo 2015: Turbine Technical Conference and Exposition, Montreal, Quebec, Canada, June 15–19, pp. 1–11.